

This is an Open Access document downloaded from ORCA, Cardiff University's institutional repository: <https://orca.cardiff.ac.uk/id/eprint/118530/>

This is the author's version of a work that was submitted to / accepted for publication.

Citation for final published version:

Prado-Gonjal, Jesús, Phillips, Matthew, Vaqueiro, Paz, Min, Gao and Powell, Anthony V. 2018. Skutterudite thermoelectric modules with high volume-power-density: scalability and reproducibility. *ACS Applied Energy Materials* 1 (11) , pp. 6609-6618. 10.1021/acsaem.8b01548

Publishers page: <http://dx.doi.org/10.1021/acsaem.8b01548>

Please note:

Changes made as a result of publishing processes such as copy-editing, formatting and page numbers may not be reflected in this version. For the definitive version of this publication, please refer to the published source. You are advised to consult the publisher's version if you wish to cite this paper.

This version is being made available in accordance with publisher policies. See <http://orca.cf.ac.uk/policies.html> for usage policies. Copyright and moral rights for publications made available in ORCA are retained by the copyright holders.



# Skutterudite Thermoelectric Modules with High Volume-Power-Density: Scalability and Reproducibility

Jesús Prado-Gonjal,<sup>‡</sup> Matthew Phillips,<sup>§</sup> Paz Vaqueiro,<sup>‡</sup> Gao Min,<sup>§\*</sup> Anthony V. Powell<sup>‡\*</sup>

<sup>‡</sup> Department of Chemistry, University of Reading, RG6 6AD, Reading, UK

<sup>§</sup> Cardiff School of Engineering, Cardiff University, The Parade, CF24 3AA, Cardiff, UK

**KEYWORDS:** Thermoelectric module, skutterudite, thermoelectric properties, high volume-power-density, waste heat recovery, energy harvesting, ball milling

## ABSTRACT

The construction and evaluation of wholly-skutterudite thermoelectric modules with a high volume-power-density is described. Such modules afford the maximum power output for the minimum use of material. Synthesis of the component n-type unfilled skutterudite  $\text{CoSb}_{2.75}\text{Sn}_{0.05}\text{Te}_{0.20}$  and p-type filled skutterudite  $\text{Ce}_{0.5}\text{Yb}_{0.5}\text{Fe}_{3.25}\text{Co}_{0.75}\text{Sb}_{12}$ , was achieved using a scalable ball-milling route that provides sufficient material for the construction and assessment of performance of 12 modules. Impedance spectroscopy at room temperature is shown to provide a rapid means of evaluating the quality of module fabrication. The results show a high degree of reproducibility in module performance across the 12 modules, with an average internal resistance

of 102(4) m $\Omega$ . Electrical measurements on the component n- and p-type materials reveal power factors ( $S^2\sigma$ ) of 1.92 and 1.33 mW m<sup>-1</sup> K<sup>-2</sup>, respectively, at room temperature and maximum figures of merit of  $ZT = 1.13$  (n-type) and  $ZT = 0.91$  (p-type) at 673 K and 823 K, respectively. The figure of merit of the module at room temperature ( $ZT = 0.12$ ) is reduced by *ca.* 39% from the average of the n- and p-type component materials at the same temperature, as a result of thermal- and electrical-contact resistance losses associated with the architecture of the module. I-V curves for the module determined for  $\Delta T$  in the range 50 – 450 K show an almost linear dependence of the open-circuit voltage on  $\Delta T$  and allow calculation of the power output, which reaches a maximum value of 1.8 W (0.9 W cm<sup>-2</sup>) at  $\Delta T = 448$  K.

## **Introduction**

Thermoelectric (TE) modules, composed of pairs of n-type and p-type semiconductors, may be used for direct thermal to electrical energy conversion. TE technology is particularly attractive for waste-heat energy harvesting in automobiles.<sup>1-4</sup> For a gasoline-engined vehicle, *ca.* 30 % of the primary gasoline energy is lost as waste heat in the exhaust gas, with a similar proportion lost in the engine-cooling system.<sup>5</sup> Using a thermoelectric generator (TEG), a proportion of this waste heat can be converted into electrical power. Furthermore, by increasing the efficiency of fossil fuel usage in combustion engines, TE technology has the potential to make an important contribution to reducing CO<sub>2</sub> and greenhouse gas emissions.<sup>6, 7-8</sup> In 1998, Nissan fabricated the first TEG for automobiles based on Si-Ge elements.<sup>9-10</sup> and subsequent generators have been constructed using modules fabricated with Bi<sub>2</sub>Te<sub>3</sub><sup>11</sup> as well as half-Heusler<sup>12</sup> and skutterudite based materials.<sup>13-14</sup> However, the most commonly-available commercial power-generating TE

modules are still currently based on Bi<sub>2</sub>Te<sub>3</sub> alloys. These modules suffer from the limitation that there is a fall-off in performance of the Bi<sub>2</sub>Te<sub>3</sub>-based materials at higher temperatures.<sup>15-16</sup> Automotive applications therefore require the development of new modules containing materials that exhibit high performance at the higher temperatures appropriate to vehicle exhaust-gas streams.

High TE performance requires materials that exhibit the combination of a low electrical resistivity ( $\rho$ ) and thermal conductivity ( $\kappa$ ) concomitantly with a high Seebeck coefficient ( $S$ ). This unusual combination of properties maximizes the figure of merit  $ZT$  (Eq. 1).

$$ZT = \frac{S^2}{\rho \kappa} T \quad (1)$$

The power factor ( $PF = S^2/\rho$ ) may be optimized by controlling the carrier concentration through doping or chemical substitution in the materials. High mobility carriers are desirable and semiconductors best fulfil these requirements, having typical carrier concentrations of  $10^{19}$  to  $10^{21}$  carriers  $\text{cm}^{-3}$ .<sup>3, 17-18</sup> The efficiency of TE energy recovery ( $\eta$ ) is related directly to this figure of merit by:

$$\eta = \left( \frac{\Delta T}{T_h} \right) \frac{\sqrt{Z\bar{T}+1}-1}{\sqrt{Z\bar{T}+1}+T_c/T_h}. \quad (2)$$

where  $\Delta T$  is the difference in temperature between the hot ( $T_h$ ) and cold ( $T_c$ ) sides of the TEG and  $Z\bar{T}$  the average figure of merit over the temperature range  $\Delta T$ . Maximising the efficiency requires both a large  $\Delta T$  and also a large average  $ZT$ .

Skutterudite-based materials are promising candidates from which to fabricate modules for high-temperature applications.<sup>13, 19-21</sup> Binary skutterudites may be formulated as  $\text{MX}_3$ , where M is a transition metal and X is an element from Group 15. The skutterudite structure consists of a framework of corner-sharing  $\text{MX}_6$  octahedra, in which there are large cages able to accommodate filler species, such as rare-earth cations (Figure 1). The fillers act as Einstein oscillators, exhibiting localised low-energy vibrational modes (often termed “rattling” vibrations), that can dramatically reduce the thermal conductivity ( $\kappa$ ) by scattering phonons, thereby reducing the lattice contribution to the thermal conductivity ( $\kappa_L$ ). It has been demonstrated that double filling,<sup>22-24</sup> as in p-type  $\text{Ce}_{0.5}\text{Yb}_{0.5}\text{Fe}_{3.25}\text{Co}_{0.75}\text{Sb}_{12}$  for example, promotes phonon scattering over a broader range of the phonon spectrum, owing to the different resonance frequencies of the Ce and Yb fillers. This effects further reductions to the lattice thermal conductivity thereby improving the TE performance.<sup>25</sup> Remarkably, the presence of Sn in the unfilled n-type skutterudite  $\text{CoSb}_{2.75}\text{Sn}_{0.05}\text{Te}_{0.20}$  also leads to enhancements in ZT.<sup>26</sup>

The best-performing skutterudites exhibit an average  $ZT = 0.5$ , which at  $\Delta T = 500\text{K}$ , corresponds to a calculated (Eq. 2) efficiency of *ca.* 8.8%. In practice, electrical and thermal contact losses associated with the construction of the module reduce this to *ca.* 7%.<sup>3, 21</sup>

Here, we describe the construction and evaluation of high-temperature TE modules containing filled and unfilled skutterudites.  $\text{CoSb}_{2.75}\text{Sn}_{0.05}\text{Te}_{0.20}$  (n-type) and  $\text{Ce}_{0.5}\text{Yb}_{0.5}\text{Fe}_{3.25}\text{Co}_{0.75}\text{Sb}_{12}$  (p-type) were synthesised by mechanochemical alloying, which offers a scalable route to the production of large quantities of material: an essential feature for the large-scale implementation of TE technology in high-volume sectors, such as automotive. In addition to structural characterization and TE property measurements, the thermal compatibility and stability in air of the n- and p-type materials are assessed. The methodology for module fabrication and rapid

screening of module quality, together with evaluation of TE performance at high temperatures ( $T_h \leq 746$  K) is described and discussed. The results demonstrate that modules are stable up to  $\Delta T=300$  K ( $T_h=575$  K) and can be operated at higher temperatures, up to  $\Delta T=400$  K ( $T_{\text{hot side}}=675$  K), for short periods with no noticeable degradation in performance.

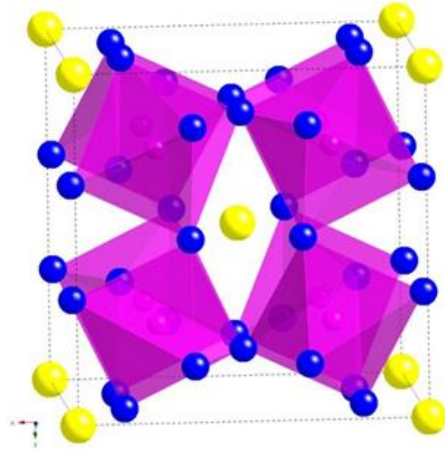


**Figure 1.** Crystal structure of a filled skutterudite.  $MX_6$  octahedra are shown in pink, with the X atoms represented by blue spheres and the filler atoms as yellow spheres.

## Experimental Section

### Material preparation

$CoSb_{2.75}Sn_{0.05}Te_{0.20}$  (n-type material) and  $Ce_{0.5}Yb_{0.5}Fe_{3.25}Co_{0.75}Sb_{12}$  (p-type material) were prepared from mixtures of the elements Co (Alfa Aesar, 99.8% powder), Sb (Alfa Aesar, 99.5% powder), Sn (Aldrich, 99.9+ % powder), Te (Aldrich, 99.99 %, granular), Ce (Alfa Aesar, 99.8% ingot), Yb (Alfa Aesar, 99.9% ingot) and Fe (Aldrich, 99.9+ % powder) of appropriate stoichiometry. The mixtures were loaded together with 13  $ZrO_2$  balls (20 mm diameter) into a 250 ml  $ZrO_2$  grinding vessel. To prevent oxidation, the vessel (equipped with a gas-tight lid) was sealed inside an Argon-filled glove-box. In the case of  $Ce_{0.5}Yb_{0.5}Fe_{3.25}Co_{0.75}Sb_{12}$ , the grinding

vessel was loaded into a Fritsch P6 Planetary Ball Mill. Grinding was carried out at 400 rpm for 10 h. For  $\text{CoSb}_{2.75}\text{Sn}_{0.05}\text{Te}_{0.20}$ , the same conditions were used, although the milling was performed using a Retsch Planetary Ball Mill PM100. This methodology allows the preparation of > 60 g of skutterudite per batch on a laboratory scale.

The ball-milled powders were loaded into a graphite die in an argon-filled glove box and consolidated by hot-pressing at 90 MPa and 873 K ( $\text{CoSb}_{2.75}\text{Sn}_{0.05}\text{Te}_{0.20}$ ) or 823 K ( $\text{Ce}_{0.5}\text{Yb}_{0.5}\text{Fe}_{3.25}\text{Co}_{0.75}\text{Sb}_{12}$ ) for 30 minutes. The consolidated pellets, used for the construction of the modules, have a diameter of 12.7 mm and a thickness of *ca.* 2.2 mm. The densities of the consolidated pellets, measured using an Archimedes balance ADAM PW184, are between 7.47 – 7.59 g cm<sup>-3</sup> for  $\text{CoSb}_{2.75}\text{Sn}_{0.05}\text{Te}_{0.20}$ , corresponding to 98.3- 99.8 % of the theoretical density. In the case of  $\text{Ce}_{0.5}\text{Yb}_{0.5}\text{Fe}_{3.25}\text{Co}_{0.75}\text{Sb}_{12}$ , these values range between 7.7 – 7.9 g cm<sup>-3</sup> (96.3 – 98.8 %).

### **Material characterization**

Temperature-dependent (300 - 673 K) powder X-ray diffraction (XRD) data were collected using a Bruker D8 Advance Powder X-ray diffractometer, operating with Ge-monochromated Cu K $\alpha$ 1 radiation ( $\lambda = 1.54046 \text{ \AA}$ ) and fitted with a LynxEye detector. A fragment of each of the skutterudite pellets was ground and the powder was placed inside a glass capillary with a diameter of 0.5 mm. Data were measured over the angular range  $10 \leq 2 \theta / ^\circ \leq 100$  for 4 hours with rotation of the capillary during the data collection. Unit-cell parameters were calculated using the Le Bail method implemented in the FullProf software package.<sup>27</sup> The peak shape was described using a pseudo-Voigt profile function and the background was fitted using linear interpolation.

The chemical composition of the samples was determined using the ICP-MS method. 50 mg of finely ground sample were digested in aqua regia in a microwave. The measurements were carried out on an Agilent 7700 instrument. A TA-Q600SDT TGA instrument was used to investigate the thermal stability in air of *ca.* 50 mg of fragment of a pellet. The samples were heated from room temperature to 873 K, at a ramp rate of 5 K min<sup>-1</sup>. Scanning Electron Microscopy (SEM) studies were carried out on the surface of sintered pellets using a FEI Quanta FEG 600 Environmental Scanning Electron Microscope, operating at a voltage of 20 kV under high vacuum.

The temperature dependence of both the electrical resistivity ( $\rho$ ) and Seebeck coefficient ( $S$ ) was measured simultaneously over the temperature range  $303 \leq T/\text{K} \leq 823$  using a Linseis LSR-3 instrument with samples contained under a partial pressure of He. A temperature gradient of 50 K was applied across the pellet for Seebeck coefficient measurements and a 100 mA current was passed for resistivity measurements.

A Netzsch LFA 447 NanoFlash instrument was employed to measure the thermal diffusivity ( $\alpha$ ) and the heat capacity ( $C_p$ ) of the samples over the temperature range of  $300 \leq T/\text{K} \leq 573$  in 25 K steps. Higher temperature measurements ( $573 \leq T/\text{K} \leq 823$  K) in 50 K steps were performed using an Anter Flashline 3000 instrument. In order to maximise the heat absorption and emission, a graphite coating was applied to the surface of the pellets. The thermal conductivity ( $\kappa$ ) was calculated using  $\kappa = \alpha C_p d$ , where  $d$  is the sample density. A reference material, Pyroceram<sup>TM</sup> 9606, was used for the determination of the heat capacity of the samples. Cowan's model with a pulse correction was applied to calculate  $\alpha$ .<sup>28</sup> The electronic ( $\kappa_e$ ) and lattice ( $\kappa_L$ ) contributions of the thermal conductivity were estimated using the electrical conductivity data in

conjunction with the Wiedemann–Franz law. The value of the Lorenz number was obtained from the equation  $L = 1.5 + \exp[-|S|/116]$ , where  $L$  is in  $10^{-8} \text{ W } \Omega \text{ K}^{-2}$  and  $S$  in  $\mu\text{V K}^{-1}$ .<sup>29</sup>

### **Module fabrication**

Modules consisting of an array of nine thermocouples were fabricated from 13 mm diameter pellets of the n-type and p-type skutterudites (Figure 2(a)). Pellets were ground and polished to a uniform thickness of approximately 2.2 mm. A metal diffusion barrier, consisting of a palladium layer followed by a nickel layer was then applied to the top and bottom surfaces via electroplating. The total thickness of the barrier layer was determined to be 10  $\mu\text{m}$  by microscopy. The pellets were cut into thermoelements using an Accutom-100 automated diamond cutting wheel, with each thermoelement having the approximate dimensions  $1.7 \times 1.7 \times 2.2$  mm. Two alumina ceramic plates ( $16 \times 13 \times 0.63$  mm) with bonded  $2 \times 5 \times 0.35$  mm copper strips (European Thermodynamics Ltd) were used to provide the thermal and electrical contacts. Junctions between the copper strips and the thermoelements were formed using the high temperature solder  $\text{Pb}_{93.5}\text{Sn}_5\text{Ag}_{1.5}$ . The joining materials have a melting point around 569 K. All of the components (i.e. thermoelements, alumina plates, and solder pieces) were assembled using a homemade stainless-steel assembly holder. To ensure a good bond, flux paste was spread between both the thermoelement/solder and solder/copper strip interfaces. The module assembly was then placed in a quartz tube, under an argon atmosphere, and the tube inserted into a tube furnace. The module assembly was heated to 623 K in order to melt the soldered joints. The holder was then removed and the module assembly allowed to cool under an argon atmosphere, before two wires were soldered to the cold side of the module to provide the electrical contacts.

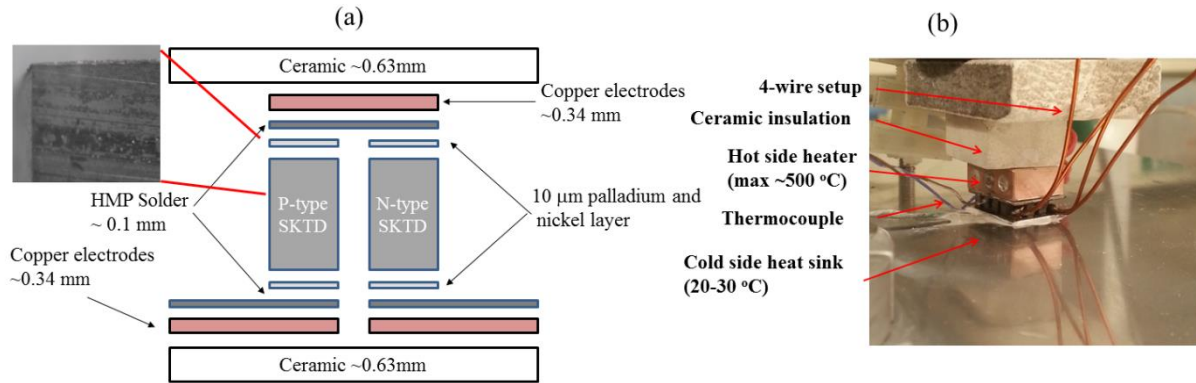


**Figure 2.** (a) Schematic diagram of the construction of a thermoelectric couple illustrating the different components. (b) Experimental set-up for module power measurements.

Skutterudite modules have an optimum operating window of around 573 - 773 K. Braze materials with a melting temperature 50-100 K higher are required to join the thermoelements to ensure stable operation. Although silver braze materials with melting temperatures above 873 K are potentially suitable, when tested at these brazing temperatures, the silver braze tended not to wet fully the surface of the n-type material, preventing a strong mechanical bond from being achieved. Although the cause of the poor wetting is not known, it may be related to the brazing occurring at temperatures higher than the consolidation temperature of the skutterudite pellet. A discolouration of the n-type elements is observed in the region of the joining area after brazing with a silver-based braze. This may indicate chemical reaction at the surface of the thermoelement that disrupts the joining process. For this reason, lead-based solders were used to fabricate the modules reported here as they enable fabrication to be achieved below the temperature at which the thermoelements are consolidated. Although this imposes an upper limit on the temperature of operation of the module, the results reported below indicate that the modules produce high volume-power-densities event at  $\Delta T = 448\text{K}$  and that efforts to understand the nature of the interaction between high-temperature silver brazes and the skutterudite

materials at elevated temperatures, which would allow the use of high-temperature brazes, would prove fruitful in achieving even higher power densities.

### **Module characterization**

Rapid screening to ensure correct assembly of the twelve fabricated modules was carried out using impedance spectroscopy. Measurements were carried out using an Autolab PGSTAT302N potentiostat with the results analysed using ZPlot software. The electrical impedance of the TE module was measured over the mHz to kHz range at room temperature. The data are described by an expression for an equivalent circuit, the variables of which are refinable parameters that allow determination of the internal resistance and the TE properties. The data provide an estimated ZT value (full details of the procedure have been published elsewhere<sup>30-32</sup>), sufficient to confirm the module quality.

Module power measurements (Figure 2(b)) were undertaken in a custom-made module-testing vacuum chamber evacuated through a turbo-molecular pump. The module was mounted to the base of the chamber using heat transfer paste, with the water-cooled base acting as the cold sink for the module. The heat source consists of a copper block with inserts for cartridge heaters that provide up to 100 W. The heater block is approximately the same size as the module to minimise thermal losses. A clamping plate is used to hold the heater block against the module with 20 mm of thermal insulation to minimise thermal losses between the heater block and the spring-loaded clamping plate. To ensure good thermal contact between the heater block and the module, graphite sheet was used to minimise any voids at the interfaces. Thermocouples (TCs) are located in indentations in the heater block and cold sink to enable measurement of the temperature at the interfaces of the heat transfer layers.

Both the module output power and heater input power measurements were taken using separate voltage and current leads to negate any resistances other than that due to the module and its connection wires. The system was evacuated, typically to  $5 \times 10^{-6}$  mbar, and once a stable pressure was achieved, a B&K Precision 9183 power supply was used to ramp the heater to a set temperature and to maintain a constant heat flow through the module. When a stable set temperature was achieved, fast I-V trace curves were taken from open-circuit to short-circuit conditions, using a Keithley 2460 source-measurement unit. The curve was taken with a scan rate of  $5 \text{ V s}^{-1}$ , to ensure a constant temperature is maintained throughout the measurement. The output voltage and module internal resistance are calculated from the curve, together with the power output of the module at that temperature.

## **Results and Discussion**

### **Structural and compositional characterization**

Powder X-ray diffraction data for the as-prepared ball-milled materials and the consolidated ball-milled materials are presented in Figure 3. It is evident that the formation mechanisms of  $\text{CoSb}_{2.75}\text{Sn}_{0.05}\text{Te}_{0.20}$  and  $\text{Ce}_{0.5}\text{Yb}_{0.5}\text{Fe}_{3.25}\text{Co}_{0.75}\text{Sb}_{12}$  differ. In the case of  $\text{Ce}_{0.5}\text{Yb}_{0.5}\text{Fe}_{3.25}\text{Co}_{0.75}\text{Sb}_{12}$ , the skutterudite phase is already present after ball milling, whereas for  $\text{CoSb}_{2.75}\text{Sn}_{0.05}\text{Te}_{0.20}$ , ball milling simply reduces the particle size of the components, as evidenced by the significant broadening of the diffraction peaks; a hot-pressing process is necessary to complete the crystallization of the skutterudite phase. Our data indicate that the formation of  $\text{CoSb}_{2.75}\text{Sn}_{0.05}\text{Te}_{0.20}$  on hot-pressing occurs below 823 K (Figure S1, Supplementary Information), but hot pressing at 873 K is required to produce consolidated pellets with densities

close to the theoretical value. SEM micrographs (Figure S2, Supplementary Information) of the consolidated materials show a dense and void-free microstructure.

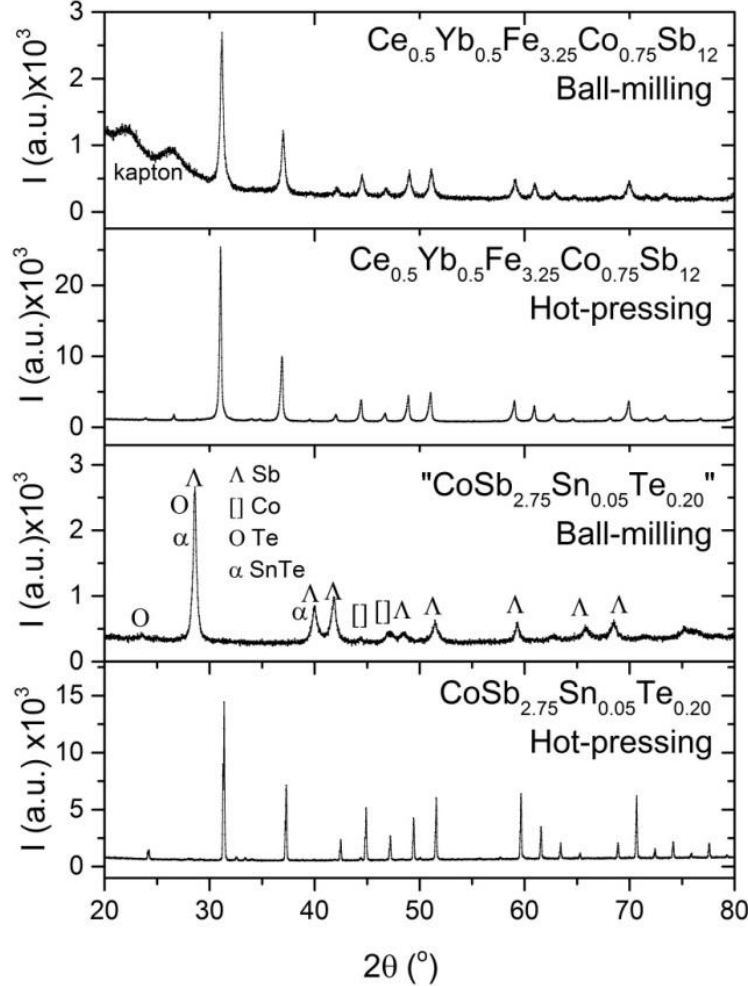


**Figure 3.** Powder X ray diffraction patterns of the as-prepared ball-milled materials and the same samples after consolidation by hot pressing.

All of the reflections in the powder diffraction patterns of the hot-pressed samples can be indexed on the basis of a cubic ( $Im\bar{3}$ ) unit cell. Lattice parameters at room temperature, obtained from Le Bail fitting, are  $a = 9.0483(1) \text{ \AA}$  and  $9.12077(9) \text{ \AA}$  for  $\text{CoSb}_{2.75}\text{Sn}_{0.05}\text{Te}_{0.20}$  and  $\text{Ce}_{0.5}\text{Yb}_{0.5}\text{Fe}_{3.25}\text{Co}_{0.7}\text{Sb}_{12}$ , respectively.

The stoichiometry of the hot-pressed samples was confirmed by ICP - MS. This yields compositions of  $\text{Co}_{0.99}\text{Sb}_{2.72}\text{Sn}_{0.05}\text{Te}_{0.20}$  and  $\text{Ce}_{0.51}\text{Yb}_{0.47}\text{Fe}_{3.13}\text{Co}_{0.79}\text{Sb}_{12.02}$ , in good agreement with the nominal stoichiometries.

### Stability in air

The thermal stability of the materials is of critical importance for devices intended to operate at elevated temperatures. The susceptibility of the materials to oxidation was investigated by thermogravimetric analysis (TGA). On heating consolidated materials in air, oxidation of  $\text{CoSb}_{2.75}\text{Sn}_{0.05}\text{Te}_{0.20}$  and  $\text{Ce}_{0.5}\text{Yb}_{0.5}\text{Fe}_{3.25}\text{Co}_{0.75}\text{Sb}_{12}$  begins above 773 K and 744 K, respectively (Figure 4). The maximum operating temperature proposed for high-temperature TE devices used to recover the waste heat from vehicle exhaust systems is around 700–773 K.<sup>33-34</sup> The stability in air of the consolidated materials established here indicates that the n- and p-type skutterudites prepared are suitable for high-temperature TE applications.

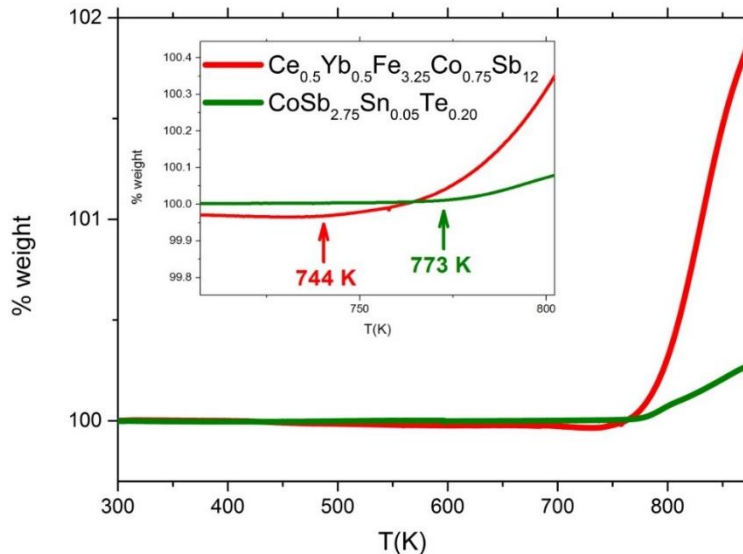


**Figure 4.** Thermogravimetric analysis (TGA) for  $\text{CoSb}_{2.75}\text{Sn}_{0.05}\text{Te}_{0.20}$  and  $\text{Ce}_{0.5}\text{Yb}_{0.5}\text{Fe}_{3.25}\text{Co}_{0.75}\text{Sb}_{12}$  pellets. The inset shows an enlargement of the region of the TGA curve

from 700 to 810 K. An increase in weight, corresponding to the onset of oxidation, can be observed above 773 K for  $\text{CoSb}_{2.75}\text{Sn}_{0.05}\text{Te}_{0.20}$  and 744 K for  $\text{Ce}_{0.5}\text{Yb}_{0.5}\text{Fe}_{3.25}\text{Co}_{0.7}\text{Sb}_{12}$ .

### Thermal expansion coefficient

Long-term stability of a TE module requires mechanical stresses in the module at the high operating temperatures to be minimised, necessitating similar thermal expansion coefficients for the n- and p-type components.<sup>35</sup> The thermal expansion coefficient ( $\alpha$ ) of a number of skutterudites have been determined;<sup>36-38</sup> the review of Rogl *et al.*<sup>39</sup> providing data for around 50 different compositions. Thermal expansion coefficients for the materials presented here were determined using lattice parameters obtained from an X-ray thermodiffraction experiment (Figure 5 and Figure S3, Supplementary information).

The thermal expansion coefficient ( $\alpha$ ) is related to the lattice parameters of a cubic material at different temperatures are to by:

$$\alpha = \frac{(a_{T_2} - a_{T_1}) / a_{T_1}}{\Delta T} \quad (3)$$

where  $a_{T_1}$  and  $a_{T_2}$  are the lattice parameters at temperatures  $T_1$  and  $T_2$ , and  $\Delta T$  corresponds to the temperature difference,  $(T_2 - T_1)$ .

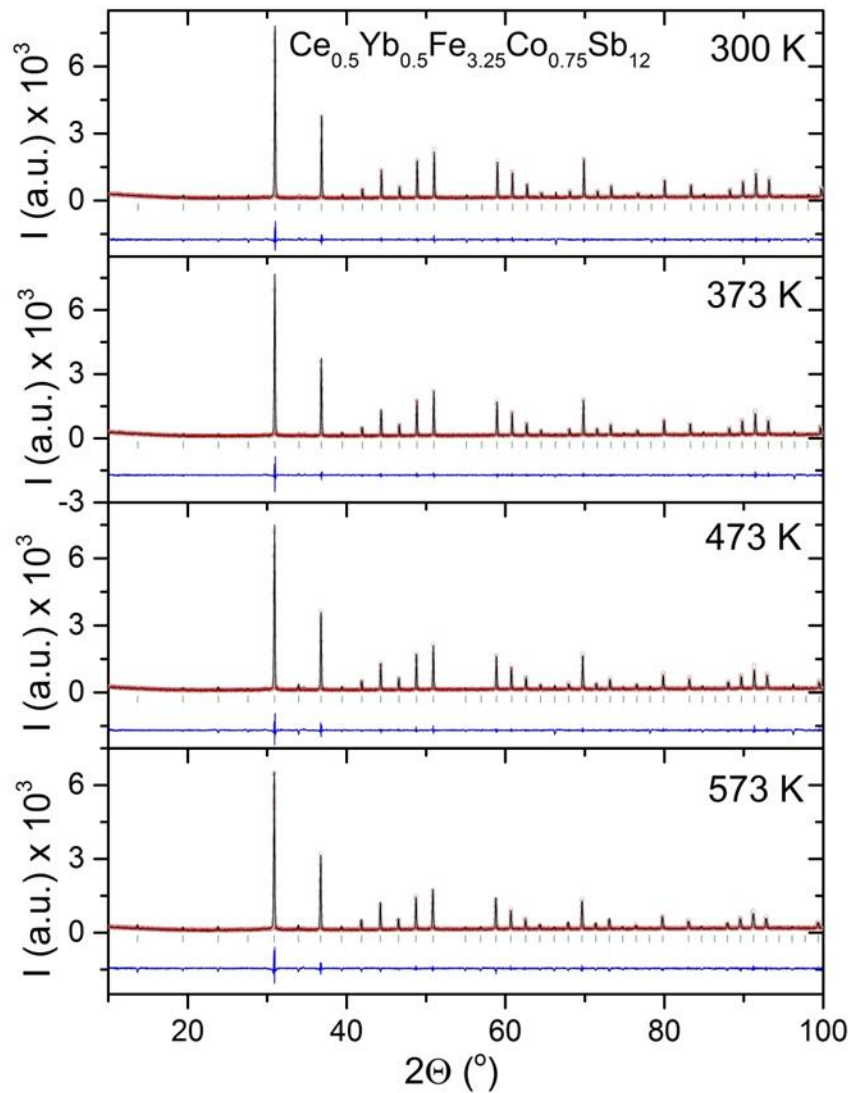


**Figure 5.** Final observed (red dotted line), calculated (black solid line) and difference (blue line) profiles for structure-independent Le Bail refinement using X-ray diffraction data for  $\text{Ce}_{0.5}\text{Yb}_{0.5}\text{Fe}_{3.25}\text{Co}_{0.75}\text{Sb}_{12}$  from room temperature to 573 K. Green markers indicate the reflection position for the skutterudite phase. Thermodiffraction data for  $\text{CoSb}_{2.75}\text{Sn}_{0.05}\text{Te}_{0.20}$  are provided as supplementary information (Figure S3).

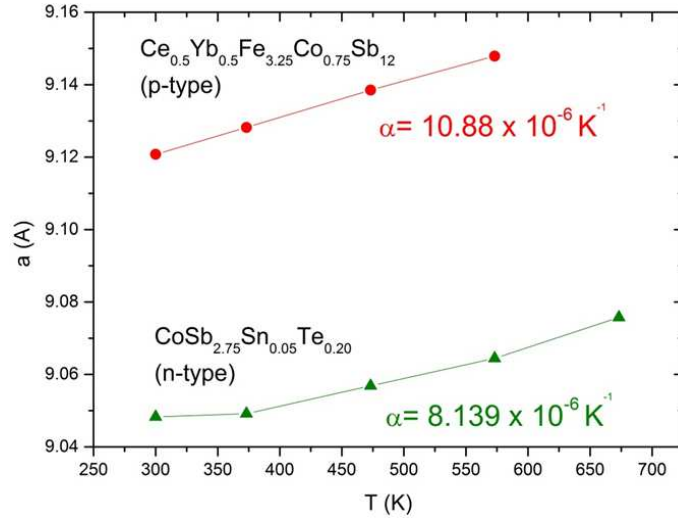


**Figure 6.** Temperature dependence of the lattice parameters obtained from Le Bail refinements using powder X-ray diffraction data.

The temperature dependence of the lattice parameters for both the n- and p-type materials (Figure 6) corresponds to a positive thermal expansion coefficient ( $\alpha$ ). The values of  $\alpha$  calculated from Eq.3 for  $\text{CoSb}_{2.75}\text{Sn}_{0.05}\text{Te}_{0.20}$  and  $\text{Ce}_{0.5}\text{Yb}_{0.5}\text{Fe}_{3.25}\text{Co}_{0.75}\text{Sb}_{12}$  are  $8.14 \times 10^{-6} \text{ K}^{-1}$  and  $10.88 \times 10^{-6} \text{ K}^{-1}$ , respectively. These values are comparable to those reported for other Sb-containing skutterudites, such as  $\text{Yb}_x\text{Co}_4\text{Sb}_{12}$  (n-type,  $\alpha = 8.17 \times 10^{-6} \text{ K}^{-1}$ ) or  $\text{Mm}_{0.7}\text{Fe}_3\text{CoSb}_{12}$  (p-type,  $\alpha = 11.33 \times 10^{-6} \text{ K}^{-1}$ ).<sup>39</sup> The similarity of the thermal expansion coefficients for both elements suggests that failure during thermal cycling due to thermal expansion mismatch is likely to be minimised.

### Thermoelectric properties of the materials

The Seebeck coefficient ( $S$ ), electrical resistivity ( $\rho$ ) and power factor (PF) for the two materials over the temperature range  $300 \leq T/\text{K} \leq 823$  are presented in Figure 7. Seebeck coefficient measurements confirm the n- and p-type character of  $\text{CoSb}_{2.75}\text{Sn}_{0.05}\text{Te}_{0.20}$  and

$\text{Ce}_{0.5}\text{Yb}_{0.5}\text{Fe}_{3.25}\text{Co}_{0.75}\text{Sb}_{12}$  respectively. For both materials, the absolute value of the Seebeck coefficient increases with temperature, reaching maximum values of  $-232 \mu\text{V K}^{-1}$  at 702 K and  $156 \mu\text{V K}^{-1}$  at 813 K, for the n- and p-type phases respectively.

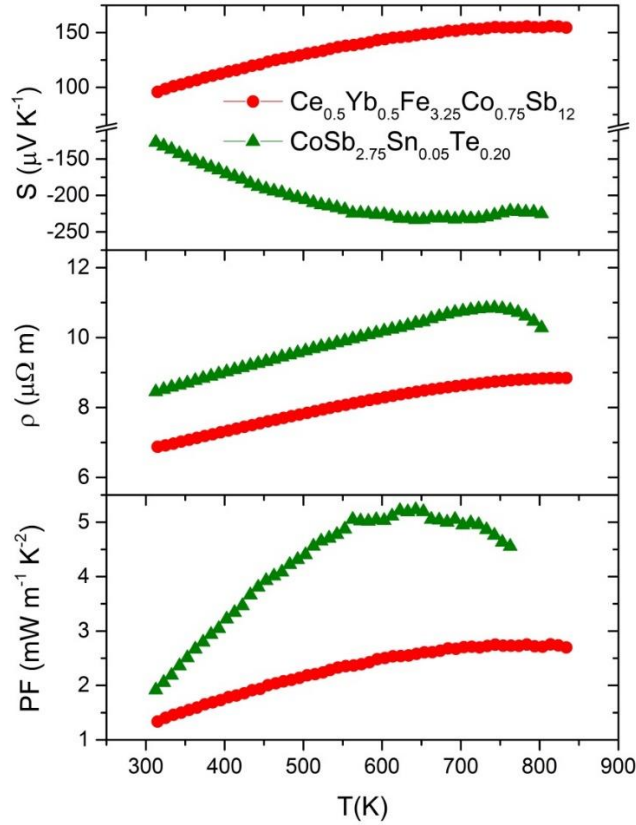


**Figure 7.** Temperature dependence of the Seebeck coefficient ( $S$ ), electrical resistivity ( $\rho$ ) and power factor ( $\text{PF} = S^2/\rho$ ) of  $\text{CoSb}_{2.75}\text{Sn}_{0.05}\text{Te}_{0.20}$  (green triangles) and  $\text{Ce}_{0.5}\text{Yb}_{0.5}\text{Fe}_{3.25}\text{Co}_{0.75}\text{Sb}_{12}$  (red circles).

The electrical resistivity of the samples (Figure 7) increases slightly with increasing temperature; behaviour reminiscent of a metal. Although the resistivity of  $\text{CoSb}_{2.75}\text{Sn}_{0.05}\text{Te}_{0.20}$  at 300 K ( $\rho \approx 8.45 \mu\Omega \text{ m}$ ) is *ca.* 22 % higher than that of  $\text{Ce}_{0.5}\text{Yb}_{0.5}\text{Fe}_{3.25}\text{Co}_{0.75}\text{Sb}_{12}$  ( $\rho \approx 6.88 \mu\Omega \text{ m}$ ), the large Seebeck coefficient of the former results in a relatively high power factor. The power factor

reaches  $5.22 \text{ mW m}^{-1} \text{ K}^{-2}$  at 640 K for  $\text{CoSb}_{2.75}\text{Sn}_{0.05}\text{Te}_{0.20}$ . This compares with a value of  $2.75 \text{ mW m}^{-1} \text{ K}^{-2}$  for  $\text{Ce}_{0.5}\text{Yb}_{0.5}\text{Fe}_{3.25}\text{Co}_{0.7}\text{Sb}_{12}$  at 813 K.

The linear region of  $S(T)$  (300 – 600 K) may be used to estimate the charge carrier concentration through the Mott formula (Eq. 4).<sup>40 41</sup> This leads to carrier concentrations of  $2.70 \times 10^{20} \text{ cm}^{-3}$  for  $\text{CoSb}_{2.75}\text{Sn}_{0.05}\text{Te}_{0.20}$  and  $1.02 \times 10^{21} \text{ cm}^{-3}$  for  $\text{Ce}_{0.5}\text{Yb}_{0.5}\text{Fe}_{3.25}\text{Co}_{0.7}\text{Sb}_{12}$ .

$$S = \frac{\pi^2 k_B^2 2m_e}{eh^2 (3n\pi^2)^{2/3}} T \quad (4)$$

The temperature dependence of the Seebeck coefficient also provides an estimate of the band gap ( $E_g$ ) through the Goldsmid and Sharp equation (Eq. 5), by considering the temperature ( $T_{max}$ ) at which the maximum value of  $|S|$  is observed ( $S_{max}$ ).<sup>42</sup> This approach leads to a band gap of  $E_g \approx 0.33 \text{ eV}$  for  $\text{CoSb}_{2.75}\text{Sn}_{0.05}\text{Te}_{0.20}$ , slightly higher than the value of  $E_g \approx 0.25 \text{ eV}$  determined for  $\text{Ce}_{0.5}\text{Yb}_{0.5}\text{Fe}_{3.25}\text{Co}_{0.7}\text{Sb}_{12}$ . Errors in band gaps determined in this way have been estimated to be up to 20 % of the calculated value.<sup>42</sup>

$$S_{max} = \frac{E_g}{2eT_{max}} \quad (5)$$

The total thermal conductivity of each material (Figure 8) is essentially invariant with temperature and significantly reduced from that of  $\text{CoSb}_3$  ( $\kappa \approx 8 - 10 \text{ W m}^{-1} \text{ K}^{-1}$  at 300 K).<sup>43-44</sup>

The slight discontinuity in the data at 573 K is due to a change in instrument used to measure thermal diffusivity in the different temperature ranges. The reduced thermal conductivity of these materials has different origins in the two materials. In the case of the unfilled skutterudite  $\text{CoSb}_{2.75}\text{Sn}_{0.05}\text{Te}_{0.20}$ , incorporation of Te and Sn at the Sb site generates significant changes in the vibrational modes and, through point defect scattering, reduces the thermal conductivity.<sup>26</sup>

Nanostructure may also play a role. By contrast, the reduction in thermal conductivity of  $\text{Ce}_{0.5}\text{Yb}_{0.5}\text{Fe}_{3.25}\text{Co}_{0.7}\text{Sb}_{12}$  is due to the presence of two filler species with different rattling frequencies that produce phonon scattering over a broad range of the phonon spectrum.<sup>22, 25</sup>

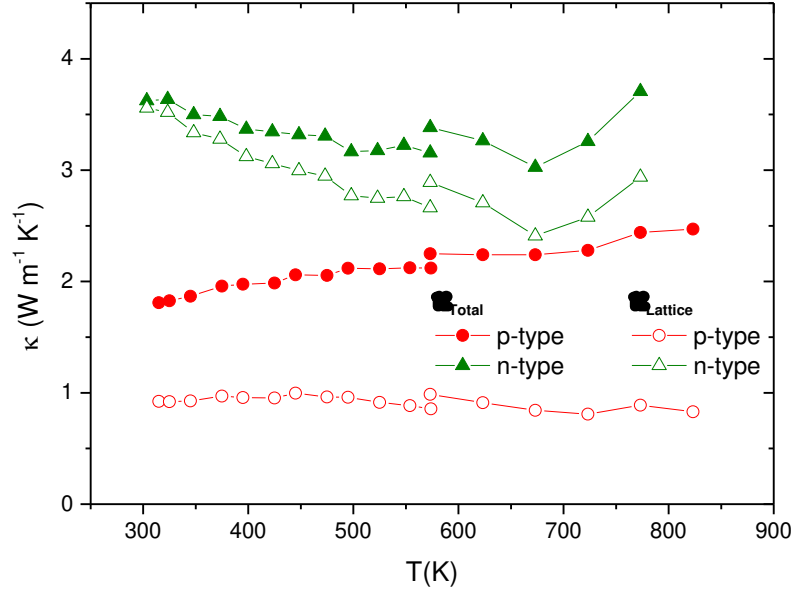


**Figure 8.** Total ( $\kappa_{\text{Total}}$ ) and lattice ( $\kappa_{\text{Lattice}}$ ) thermal conductivity of n-type  $\text{CoSb}_{2.75}\text{Sn}_{0.05}\text{Te}_{0.20}$  (green triangles) and p-type  $\text{Ce}_{0.5}\text{Yb}_{0.5}\text{Fe}_{3.25}\text{Co}_{0.7}\text{Sb}_{12}$  (red circles) as a function of temperature.

The maintenance of a high power factor, combined with a reduced thermal conductivity, produces a relatively high figure of merit,  $ZT$ . In both materials,  $ZT$  increases with increasing temperature (Figure 9), reaching maximum values of 1.13 at 673 K and 0.91 at 823 K for  $\text{CoSb}_{2.75}\text{Sn}_{0.05}\text{Te}_{0.20}$  and  $\text{Ce}_{0.5}\text{Yb}_{0.5}\text{Fe}_{3.25}\text{Co}_{0.7}\text{Sb}_{12}$  respectively. It is notable that the figure of the merit of the latter is still rising at the highest temperature investigated.

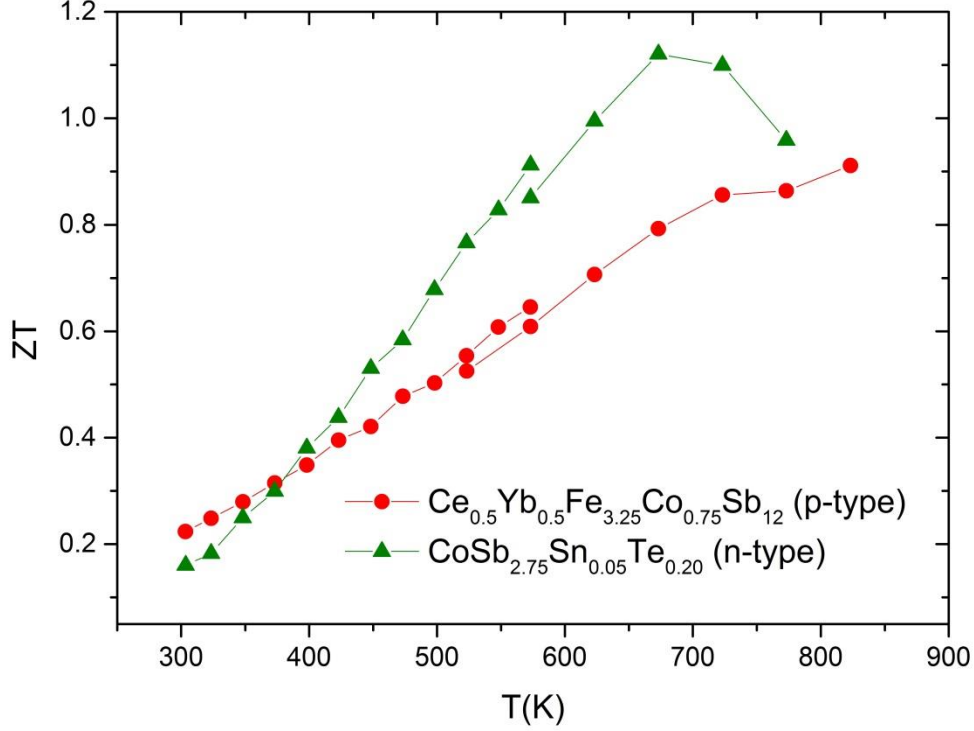


**Figure 9.** Temperature dependence of the figure of merit,  $ZT$ , of the n-type  $\text{CoSb}_{2.75}\text{Sn}_{0.05}\text{Te}_{0.20}$  (green triangles) and p-type  $\text{Ce}_{0.5}\text{Yb}_{0.5}\text{Fe}_{3.25}\text{Co}_{0.75}\text{Sb}_{12}$  (red circles) skutterudites.

### Module properties

Twelve modules were fabricated and screened using impedance spectroscopy. The impedance plot (Figure 10) for a skutterudite module constructed from  $\text{CoSb}_{2.75}\text{Sn}_{0.05}\text{Te}_{0.20}$  and  $\text{Ce}_{0.5}\text{Yb}_{0.5}\text{Fe}_{3.25}\text{Co}_{0.75}\text{Sb}_{12}$  shows the typical ‘Warburg like’ shape, characteristic of a TE module. The total impedance  $Z(j\omega)$  of the equivalent circuit,<sup>30-31</sup> shown as an inset to Figure 10, is given by,

$$Z(j\omega) = L + R + \frac{1}{Z_{W_a}^{-1} + Z_{W_{CT}}^{-1}}. \quad (6)$$

where,  $L$  is the inductance,  $R$  is the internal resistance of the module,  $W_a$  is the adiabatic Warburg impedance associated with the contacts and  $W_{CT}$  is a constant-temperature Warburg impedance

associated with the TE effect. The two Warburg impedances are described by equations (7) and (8),

$$Z_{W_a}(j\omega) = R_C \left(\frac{j\omega}{\omega_C}\right)^{-0.5} \coth\left\{\left(\frac{j\omega}{\omega_C}\right)^{0.5}\right\} \quad (7)$$

$$Z_{W_{CT}}(j\omega) = R_{TE} \left(\frac{j\omega}{\omega_{TE}}\right)^{-0.5} \tanh\left\{\left(\frac{j\omega}{\omega_{TE}}\right)^{0.5}\right\} \quad (8)$$

where  $R_C$  and the  $R_{TE}$  are the resistances associated with the contacts and TE responses respectively and  $\omega_C$  and  $\omega_{TE}$  are the characteristic angular frequencies. The four parameters, presented in Table 1, were obtained by fitting Eq. (6) to the experimental data of Figure 10.

**Table 1.** Parameters derived from the fit of Eq. (6) to the impedance data of a TE module, presented in Figure 10.

| <b>R/mΩ</b>              | <b>R/% error</b>             | <b>R<sub>TE</sub>/mΩ</b>                | <b>R<sub>TE</sub>/% error</b> | <b>ω<sub>TE</sub>/rads<sup>-1</sup></b> | <b>ω<sub>TE</sub>/% error</b> |
|--------------------------|------------------------------|---|-------------------------------|---|-------------------------------|
| 95                       | 0.09                         | 10.6                                    | 4.10                          | 1.14                                    | 2.40                          |
|                          |                              |   |                               |   |                               |
| <b>R<sub>C</sub>/ mΩ</b> | <b>R<sub>C</sub>/% error</b> | <b>ω<sub>C</sub>/ rads<sup>-1</sup></b> | <b>ω<sub>C</sub>/% error</b>  | <b>L/nH</b>                             | <b>L/% error</b>              |
| 0.922                    | 24.2                         | 0.48                                    | 17.9                          | 98                                      | 37.4                          |

It has been shown previously<sup>30-31</sup> that  $R_{TE} = 2NS^2T\ell/\kappa A$  where  $S$ ,  $T$  and  $\kappa$  have their usual meanings,  $N$  is the number of thermocouples in the module and  $\ell$  and  $A$  are the length and cross-

sectional area of each thermoelement. It follows that an approximate  $ZT$  value for the module may be obtained from the following relation;

$$\frac{R_{TE}}{R} = 2N \frac{S^2 \ell}{\kappa AR} T = Z_{mod} T \quad (9)$$

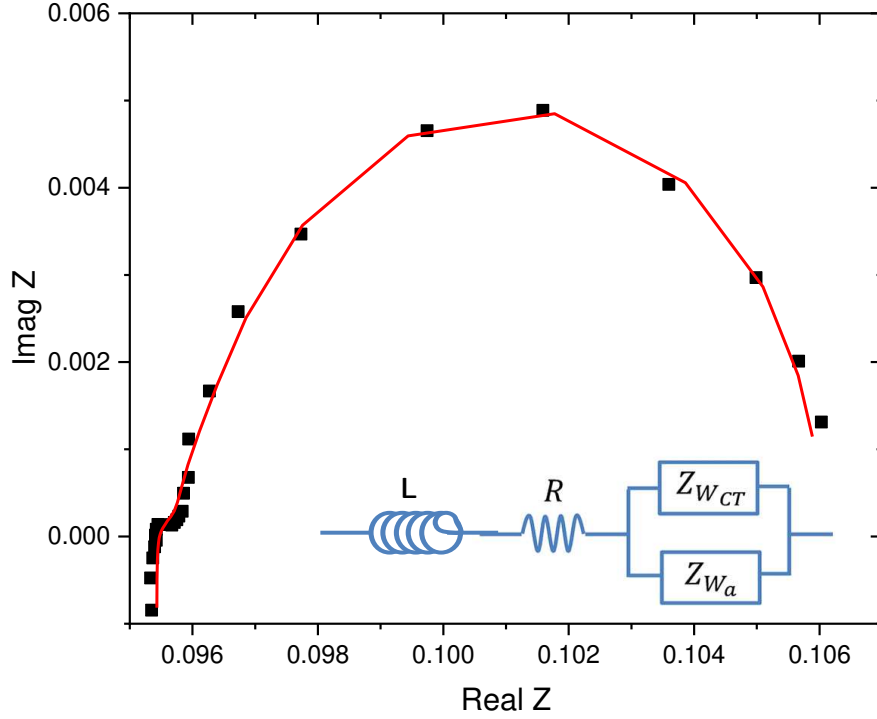


**Figure 10.** Impedance spectrum (black squares) for a skutterudite module from 5 mHz to 10 kHz. The equivalent circuit for a TE module is shown as an inset and is used to generate the fit (red line) from which the module internal resistance and  $ZT$  at room temperature are calculated. The equivalent circuit consists of a resistor  $R$  and an inductor  $L$  in series with two impedances in parallel.  $R$  is the internal resistance of the module,  $W_a$  is the adiabatic Warburg impedance associated with the module contacts and  $W_{CT}$  is the constant temperature Warburg impedance associated with the TE effect.<sup>30-31</sup>

Based on the fit to the data of Figure 10, the internal resistance of the module is determined as 95 m $\Omega$ . Using this value and the measured resistivity values of the n-type and p-type materials, the room temperature contact resistivity is estimated as *ca.* 10  $\mu\Omega$  cm<sup>2</sup>. The room-temperature figure of merit for the module has been estimated as  $ZT = 0.11$ , using Eq. (9). This is reduced by *ca.* 39% from the average value of  $ZT = 0.18$  determined experimentally (Figure 9) for the n- and p-type materials at the same temperature, owing to losses associated with the ceramic plates of the module. In order to verify that the difference in  $ZT$  between that of the component n- and p-type materials and that of the module is due to contact losses and not experimental error,  $ZT$  was also calculated using the efficiency determined from a constant heat flux I-V curve (Supporting Information). Using this technique, a value of  $ZT \sim 0.12$  is obtained, in excellent agreement with that determined above from resistivity data. The average internal resistance value for all the modules investigated is  $101 \pm 1$  m $\Omega$  and their average figure-of-merit is  $ZT = 0.12 \pm 0.01$ . The low standard deviation in these values is consistent with a high degree of reproducibility in module properties across the 12 modules fabricated. The module  $Z\bar{T}$  value was verified using an efficiency calculation from a constant heat flow I-V curve (Supporting Information).

The module current-voltage (I-V) curves (Figure 11a) were obtained under constant temperature conditions for a series of temperature differences across the module, using a scan rate of 5 V s<sup>-1</sup>. There was no detectable drop in the hot-side temperature after the measurement was taken. There is an approximately linear relationship between open circuit voltage and  $\Delta T$  up to  $\Delta T=400$  K. Although a further increase in open-circuit voltage is observed at  $\Delta T=448$  K, this is less than expected based on the linear dependence established at lower temperatures. At this temperature difference, the hot-side temperature is *ca.* 746 K, well above the melting point of the solder (570 K) used to fabricate the module, suggesting that a failure at the skutterudite-electrode interface

may be responsible for the loss of performance. Figure 11b shows the output power and internal resistance for the module at each of the temperature differences. Although there are long term stability issues with working at temperatures in excess of the solder melting temperature, the results suggest measurements on short timescales are possible and can be used to benchmark the performance of future higher temperature brazes. The maximum power output achieved for the module is *ca.* 1.85 W ( $0.9 \text{ Wcm}^{-2}$ ) at  $\Delta T = 448 \text{ K}$ . This is much higher than the values previously reported by García-Cañadas *et al.*<sup>13</sup> for a module constructed exclusively from single filled n- and p-type skutterudites.

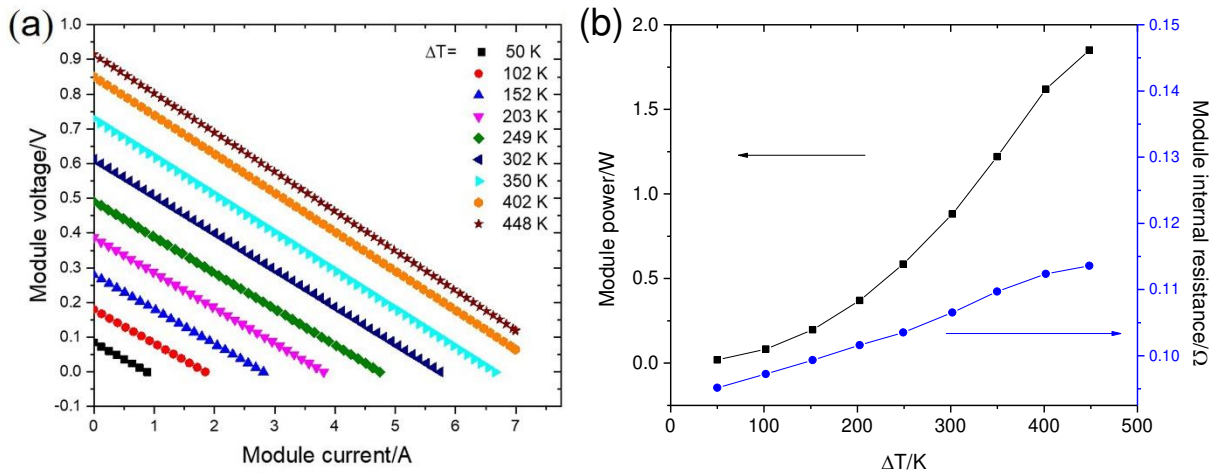


**Figure 11.** Module characteristics of a representative skutterudite module from  $\Delta T=50 \text{ K}$  to  $\Delta T=448 \text{ K}$ . (a) I-V curves taken under constant temperature conditions with a voltage scan rate of  $5 \text{ V s}^{-1}$ . (b) Module internal resistance (blue circles) and output power (black squares) for each of the applied temperature differences.

Further increases in output would be possible if a braze capable of operating at higher temperatures was used at the hot-side junctions of the module. The surface- and volume-power-

densities as a function of temperature difference for the module described here, are compared with those of other skutterudite (Sktd) modules<sup>13,21</sup> and modules constructed from materials such as SiGe<sup>45</sup>, Bi<sub>2</sub>Te<sub>3</sub><sup>46</sup> and Half-Heuslers (HH)<sup>12</sup> in Figure 12. Interestingly, the skutterudite module reported by Ochi *et al.*<sup>20</sup> has one of the lowest volume-power-densities but one of the highest surface-power-densities. This apparent contradiction may arise from efforts to improve the efficiency by increasing the leg length and cross-sectional area, thereby mitigating the effect of electrical contact losses. This comes at the expense of increased material usage and hence, a lower volume-power-density.

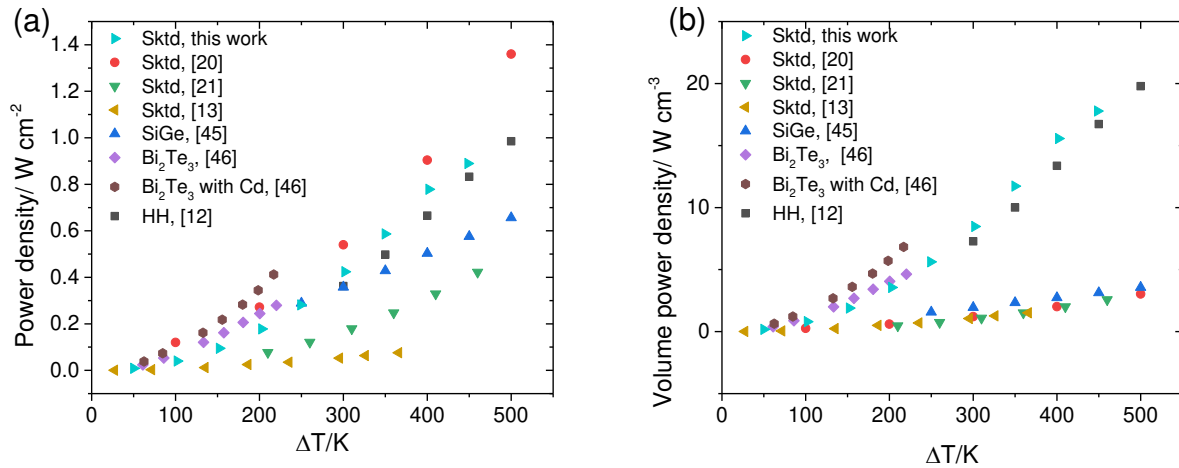


**Figure 12.** (a) Module surface-power-density and (b) volume-power-density as a function of temperature difference  $\Delta T$ , for the module described in this work together with published data for high-temperature modules. The surface-power-density is the power output divided by the area in physical contact with the heat source. The volume-power-density is the output power divided by the total volume of the thermoelements of which the module is comprised. Sktd. and HH refer respectively to modules constructed from skutterudite and half-Heuslers.

The module characterized in the present work has a high volume-power-density, affording more efficient use of material to generate a given power, a critical factor for large scale applications. More efficient use of material reduces the cost per watt for the module, but potentially limits the heat-power conversion efficiency, which we have estimated to be ca. 3 - 4% under a temperature gradient of 362 K (Figure S5, Supplementary Information). Therefore, future work will seek to optimise the module geometry for applications such as automotive waste heat recovery, where a limited amount of heat flux is available. The performance of the module described here could be enhanced further by increasing the thermoelement length and cross-sectional area to increase the power output and efficiency. Furthermore, more robust barrier coatings are needed to allow brazing and extended operation at higher temperatures.

## Conclusions

By adopting a holistic approach incorporating elements of materials design, considerations of scale-up of materials preparation, module construction and screening, we have succeeded in producing a batch of high-temperature skutterudite-based TE modules, with a high volume-power-density and reproducible TE characteristics. We describe a ball-milling process for the production of large (> 60 g) of n- and p-type skutterudites with  $ZT \sim 1$  at elevated temperatures. We also show that impedance spectroscopy performed at room temperature provides an effective means of screening module performance in an efficient and effective manner. A maximum power output of 1.8 W, equivalent to  $0.9 \text{ W cm}^{-2}$ , is achieved at  $\Delta T = 448 \text{ K}$ . The upper limit of  $\Delta T$  is determined by the melting point of the lead-based solder used for the electrical connections. Preliminary investigations with a high-temperature silver-based braze provide

evidence for reaction between the braze and the thermoelement, that weakens the mechanical bonding. Future investigation will focus on understanding the nature of this interaction, and identifying brazes able to withstand higher temperatures, whilst providing an effective mechanical join and low electrical contact resistance. This would enable higher temperature operation of the module and increased output power.

## ASSOCIATED CONTENT

**Supporting Information.** X-ray diffraction data for  $\text{CoSb}_{2.75}\text{Sn}_{0.05}\text{Te}_{0.20}$  consolidated at different temperatures, SEM micrographs of consolidated pellets, variable temperature X-ray diffraction data with Le Bail fits for  $\text{CoSb}_{2.75}\text{Sn}_{0.05}\text{Te}_{0.20}$ , the alternative method for calculating  $Z\bar{T}$  and plots of efficiency as a function of temperature difference (PDF).

## AUTHOR INFORMATION

### Corresponding Author

\*E-mail for AVP: [a.v.powell@reading.ac.uk](mailto:a.v.powell@reading.ac.uk)

\*E-mail for GM: [min@cardiff.ac.uk](mailto:min@cardiff.ac.uk)

### Author Contributions

The manuscript was written through contributions of all authors. All authors have given approval to the final version of the manuscript.

### Funding Sources

UK Engineering and Physical Sciences Council (EP/K019767/1)

## ACKNOWLEDGMENT

The authors wish to thank the UK Engineering and Physical Sciences Council (EP/K019767/1) for financial support and The University of Reading for access to the Chemical Analysis Facility for powder X-ray diffraction and Thermogravimetric Analysis. The authors would like to thank Johnson Matthey (JM Technology Centre, Sonning Common, UK) for carrying out ICP measurements.

## REFERENCES

- (1) Bell, L. E. Cooling, Heating, Generating Power, and Recovering Waste Heat with Thermoelectric Systems. *Science* **2008**, *321*, 1457-1461.
- (2) Majumdar, A. Thermoelectricity in Semiconductor Nanostructures. *Science* **2004**, *303*, 777-778.
- (3) Snyder, G. J.; Toberer, E. S. Complex Thermoelectric Materials. *Nat. Mater.* **2008**, *7*, 105-114.
- (4) Park, S. H.; Jin, Y.; Cha, J.; Hong, K.; Kim, Y.; Yoon, H.; Yoo, C.-Y.; Chung, I. High-Power-Density Skutterudite-Based Thermoelectric Modules with Ultralow Contact Resistivity Using Fe–Ni Metallization Layers. *ACS Appl. Energy Mater.* **2018**, *1*, 1603-1611.
- (5) Chiwanga, S.; Tuley, R.; Placha, K.; Robbins, M.; Gilchrist, B.; Simpson, K. Automotive Power Harvesting/Thermoelectric Applications. In *Thermoelectric Materials and Devices*, Nandhakumar, I.; White, N. M.; Beeby, S., Eds.; Royal Society of Chemistry: 2016; pp 230-251.

- (6) Orr, B. G.; Akbarzadeh, A.; Lappas, P. Reducing Automobile CO<sub>2</sub> Emissions with an Exhaust Heat Recovery System Utilising Thermoelectric Generators and Heat Pipes. SAE Technical Paper 2015-01-0051, 2015
- (7) Mori, M.; Yamagami, T.; Oda, N.; Hattori, M.; Sorazawa, M.; Haraguchi, T. Current Possibilities of Thermoelectric Technology Relative to Fuel Economy. SAE Technical Paper 2009-01-0170, 2009
- (8) Yang, J.; Stabler, F. R. Automotive Applications of Thermoelectric Materials. *J. Electron. Mater.* **2009**, *38*, 1245-1251.
- (9) Hsu, C.-T.; Yao, D.-J.; Ye, K.-J.; Yu, B. Renewable Energy of Waste Heat Recovery System for Automobiles. *J. Renewable Sustainable Energy* **2010**, *2*, 013105.
- (10). Ikoma, K.; Munekiyo, M.; Furuya, K.; Kobayashi, M.; Izumi, T.; Shinohara, K. in *Thermoelectric Module and Generator for Gasoline Engine Vehicles*, XVII International Conference on Thermoelectrics, 1998. Proceedings ICT 98., 24-28 May 1998; 1998; pp 464-467.
- (11) Bass, J. C.; Elsner, N. B.; Leavitt, F. A. Performance of the 1 kW Thermoelectric Generator for Diesel Engines, *AIP Conf. Proc.*, AIP: 1994; pp 295-298.
- (12) Zhang, Y.; Cleary, M.; Wang, X.; Kempf, N.; Schoensee, L.; Yang, J.; Joshi, G.; Meda, L. High-Temperature and High-Power-Density Nanostructured Thermoelectric Generator for Automotive Waste Heat Recovery. *Energ. Convers. Manage.* **2015**, *105*, 946-950.
- (13) García-Cañadas, J.; Powell, A. V.; Kaltzoglou, A.; Vaqueiro, P.; Min, G. Fabrication and Evaluation of a Skutterudite-Based Thermoelectric Module for High-Temperature Applications. *J. Electron. Mater.* **2013**, *42*, 1369-1374.

- (14) LaGrandeur, J.; Crane, D.; Hung, S.; Mazar, B.; Eder, A. Automotive Waste Heat Conversion to Electric Power using Skutterudite, TAGS, PbTe and BiTe, Proceedings of the 25<sup>th</sup> International Conference on Thermoelectrics, IEEE: 2006; pp 343-348.
- (15) Yang, J. Potential Applications of Thermoelectric Waste Heat Recovery in the Automotive Industry. Proceedings of the 24<sup>th</sup> International Conference on Thermoelectrics, 2005; pp 170-174.
- (16) Gao, M.; Rowe, D. M. Ring-Structured Thermoelectric Module. *Semicond. Sci. Technol.* **2007**, *22*, 880.
- (17) Barnard, R. D. *Thermoelectricity in Metals and Alloys*. Halsted Press: 1972.
- (18) Wood, C. Materials for Thermoelectric Energy Conversion. *Rep. Prog. Phys.* **1988**, *51*, 459.
- (19) Guo, J. Q.; Geng, H. Y.; Ochi, T.; Suzuki, S.; Kikuchi, M.; Yamaguchi, Y.; Ito, S. Development of Skutterudite Thermoelectric Materials and Modules. *J. Electron. Mater.* **2012**, *41*, 1036-1042.
- (20) Ochi, T.; Nie, G.; Suzuki, S.; Kikuchi, M.; Ito, S.; Guo, J. Q., Power-Generation Performance and Durability of a Skutterudite Thermoelectric Generator. *J. Electron. Mater.* **2014**, *43*, 2344-2347.
- (21) Salvador, J. R.; Cho, J. Y.; Ye, Z.; Moczygemba, J. E.; Thompson, A. J.; Sharp, J. W.; Koenig, J. D.; Maloney, R.; Thompson, T.; Sakamoto, J.; Wang, H.; Wereszczak, A. A. Conversion Efficiency of Skutterudite-Based Thermoelectric Modules. *Phys. Chem. Chem. Phys.* **2014**, *16*, 12510-12520.
- (22) Shi, X.; Yang, J.; Salvador, J. R.; Chi, M.; Cho, J. Y.; Wang, H.; Bai, S.; Yang, J.; Zhang, W.; Chen, L. Multiple-Filled Skutterudites: High Thermoelectric Figure of Merit through Separately Optimizing Electrical and Thermal Transports. *J. Am. Chem. Soc.* **2011**, *133*, 7837-7846.

- (23) Shi, X.; Salvador, J. R.; Yang, J.; Wang, H. Thermoelectric Properties of n-Type Multiple-Filled Skutterudites. *J. Electron. Mater.* **2009**, *38*, 930-933.
- (24) Shi, X.; Kong, H.; Li, C.-P.; Uher, C.; Yang, J.; Salvador, J. R.; Wang, H.; Chen, L.; Zhang, W. Low Thermal Conductivity and High Thermoelectric Figure of Merit in n-Type  $Ba_xYb_yCo_4Sb_{12}$  Double-Filled Skutterudites. *Appl. Phys. Lett.* **2008**, *92*, 182101.
- (25) Prado-Gonjal, J.; Vaquero, P.; Nuttall, C.; Potter, R.; Powell, A. V. Enhancing the Thermoelectric Properties of Single and Double Filled p-Type Skutterudites Synthesized by an Up-Scaled Ball-Milling Process. *J. Alloy. Comp.* **2017**, *695*, 3598-3604.
- (26) Liu, W.-S.; Zhang, B.-P.; Zhao, L.-D.; Li, J.-F. Improvement of Thermoelectric Performance of  $CoSb_{3-x}Te_x$  Skutterudite Compounds by Additional Substitution of IVB-Group Elements for Sb. *Chem. Mater.* **2008**, *20*, 7526-7531.
- (27) Rodriguez-Carvajal, J. FULLPROF: a Program for Rietveld Refinement and Pattern Matching Analysis. Abstracts of the Satellite Meeting on Powder diffraction of the XV Congress of the IUCr **1990**, p. 127.
- (28) Cowan, R. D. Pulse Method of Measuring Thermal Diffusivity at High Temperatures. *J. Appl. Phys.* **1963**, *34*, 926-927.
- (29) Kim, H.-S.; Gibbs, Z. M.; Tang, Y.; Wang, H.; Snyder, G. J. *APL Materials*, **2015**, *3*, 041506.
- (30) Garcia-Canadas, J.; Min, G. Impedance Spectroscopy Models for the Complete Characterization of Thermoelectric Materials. *J. Appl Phys.* **2014**, *116*, 174510.
- (31) García-Cañadas, J.; Min, G. Thermal Dynamics of Thermoelectric Phenomena from Frequency Resolved Methods. *AIP Adv.* **2016**, *6*, 035008.

- (32) Beltrán-Pitarch, B.; Prado-Gonjal, J.; Powell, A. V.; Ziolkowski, P.; García-Cañadas, J. Thermal Conductivity, Electrical Resistivity, and Dimensionless Figure of Merit (ZT) Determination of Thermoelectric Materials by Impedance Spectroscopy up to 250° C. *J. Appl. Phys* **2018**, *124*, 025105.
- (33) Sklad, A. C.; Gaultois, M. W.; Grosvenor, A. P. Examination of CeFe<sub>4</sub>Sb<sub>12</sub> upon Exposure to Air: Is This Material Appropriate for Use in Terrestrial, High-Temperature Thermoelectric Devices? *J. Alloys Compd.* **2010**, *505*, L6-L9.
- (34) Park, K.-H.; You, S.-W.; Ur, S.-C.; Kim, I.-H.; Choi, S.-M.; Seo, W.-S., High-Temperature Stability of Thermoelectric Skutterudite In<sub>0.25</sub>Co<sub>3</sub>FeSb<sub>12</sub>. *J. Electron. Mater.* **2012**, *41*, 1051-1056.
- (35) Ni, J. E.; Case, E. D.; Schmidt, R. D.; Wu, C.-I.; Hogan, T. P.; Trejo, R. M.; Kirkham, M. J.; Lara-Curzio, E.; Kanatzidis, M. G. The Thermal Expansion Coefficient as a Key Design Parameter for Thermoelectric Materials and its Relationship to Processing-Dependent Bloating. *J. Mater. Sci.* **2013**, *48*, 6233-6244.
- (36) Ravi, V.; Firdosy, S.; Caillat, T.; Brandon, E.; Van Der Walde, K.; Maricic, L.; Sayir, A. Thermal Expansion Studies of Selected High-Temperature Thermoelectric Materials. *J. Electron. Mater.* **2009**, *38*, 1433-1442.
- (37) Sekine, C.; Shimaya, Y.; Shirotani, I.; Haen, P. Thermal Expansion of Filled Skutterudite Compound SmRu<sub>4</sub>P<sub>12</sub>. *J Phys. Soc. Jpn.* **2005**, *74*, 3395-3396.
- (38) Oeschler, N.; Gegenwart, P.; Steglich, F.; Frederick, N.; Bauer, E.; Maple, M. Thermal Expansion of the Skutterudite Superconductor PrOs<sub>4</sub>Sb<sub>12</sub>. *Acta Phys. Pol. A* **2003**, *34*, 959-962.

- (39) Rogl, G.; Zhang, L.; Rogl, P.; Grytsiv, A.; Falmbigl, M.; Rajs, D.; Kriegisch, M.; Müller, H.; Bauer, E.; Koppensteiner, J. Thermal Expansion of Skutterudites. *J. Appl. Phys.* **2010**, *107*, 043507.
- (40) Mott, N. F.; Jones, H. *The theory of the properties of metals and alloys*. Courier Corporation: 1958.
- (41) Rogl, G.; Grytsiv, A.; Melnychenko-Koblyuk, N.; Bauer, E.; Laumann, S.; Rogl, P. Compositional Dependence of the Thermoelectric Properties of  $(\text{Sr}_x\text{Ba}_x\text{Yb}_{1-2x})_y\text{Co}_4\text{Sb}_{12}$  Skutterudites. *J. Phys.: Condens. Matter* **2011**, *23*, 275601.
- (42) Goldsmid, H. J.; Sharp, J. W. Estimation of the Thermal Band Gap of a Semiconductor from Seebeck Measurements. *J. Electron. Mater.* **1999**, *28*, 869-872.
- (43) Sharp, J. W.; Jones, E. C.; Williams, R. K.; Martin, P. M.; Sales, B. C. Thermoelectric Properties of  $\text{CoSb}_3$  and Related Alloys. *J. Appl. Phys.* **1995**, *78*, 1013-1018.
- (44) Toprak, M. S.; Stiewe, C.; Platzek, D.; Williams, S.; Bertini, L.; Müller, E.; Gatti, C.; Zhang, Y.; Rowe, M.; Muhammed, M. The Impact of Nanostructuring on the Thermal Conductivity of Thermoelectric  $\text{CoSb}_3$ . *Adv. Funct. Mater.* **2004**, *14*, 1189-1196.
- (45) Romanjek, K.; Vesin, S.; Aixala, L.; Baffie, T.; Bernard-Granger, G.; Dufourcq, J. High-Performance Silicon–Germanium-Based Thermoelectric Modules for Gas Exhaust Energy Scavenging. *J. Electron. Mater.* **2015**, *44*, 2192-2202.
- (46) Hao, F.; Qiu, P.; Tang, Y.; Bai, S.; Xing, T.; Chu, H.-S.; Zhang, Q.; Lu, P.; Zhang, T.; Ren, D. High Efficiency  $\text{Bi}_2\text{Te}_3$ -Based Materials and Devices for Thermoelectric Power Generation between 100 and 300°C. *Energ. Environ. Sci.* **2016**, *9*, 3120-3127.

## Table of Contents Graphic

